

Multimodal Confocal Microscopy For Diagnosing Nonmelanoma Skin Cancers

Munir Y. Al-Arashi, MD, PhD,^{1,2,3} Elena Salomatina, MS,^{2,3} and Anna N. Yaroslavsky, PhD^{1,2,3*}

¹Harvard Medical School, Boston, Massachusetts 02114

²Massachusetts General Hospital, Boston, Massachusetts 02114

³Wellman Center for Photomedicine, Boston, Massachusetts 02114

Background and Significance: The standard diagnostic procedure for skin cancers is invasive biopsy followed by histopathological evaluation. The biopsy may result in scarring and infection. A reliable way to noninvasively image suspicious lesions with high resolution and contrast would be valuable. In this study, the suitability of dye-enhanced multimodal confocal microscopy for the detection of nonmelanoma skin cancers was evaluated.

Materials and Methods: For the experiments we used fresh tumor material stained using 0.2 mg/ml or 0.05 mg/ml aqueous solutions of methylene blue (MB) or toluidine blue (TB), respectively. Reflectance, fluorescence, and fluorescence polarization images of skin specimens stained with MB and TB were excited by 656 nm and 633 nm light, respectively. Fluorescence emission and anisotropy were registered between 690 nm and 710 nm. In addition, reference reflectance images at 830 nm were acquired. In total we imaged, analyzed, and compared to histology at least 10 samples of each tumor-type including nodular basal cell carcinoma (BCC), infiltrative basal cell carcinoma, and squamous cell carcinoma (SCC).

Results and Conclusion: The morphological features and appearance of skin structures in the fluorescence images correlate well with corresponding histology for all investigated tumor-types. Multi-spectral reflectance images provide information on the tissue spectral responses and are complimentary to the fluorescence images. The differences detected by fluorescence polarization in cancerous and normal structures may be used for cancerous tissue discrimination. Our results indicate the feasibility of using multimodal confocal microscopy as real-time tool for detecting skin pathology. *Lasers Surg. Med.* 39:696–705, 2007. © 2007 Wiley-Liss, Inc.

Key words: contrast agents; fluorescence; optical pathology; polarization; reflectance

INTRODUCTION

Real time identification of malignant cells and small tumor nests is one of the major challenges in oncology. Due to the unprecedented resolution, comparable to that of histopathology, confocal microscopy has a potential for solving this problem. This potential was recognized more than 10 years ago. Since then there have been numerous attempts to use this technology as an aid in diagnostics

[1–3] and treatment guidance [4–7] of skin cancers. Endogenous (melanin [8–10]) and exogenous (aluminum chloride [4] and acetic acid [5]) contrast agents provide strong contrast in scattering, thus facilitating the process of detecting pathology. However, morphological appearance of skin structures in the images differs significantly from that in histopathology. These differences complicate the image interpretation by pathologists and impede the translation of this promising optical technique into clinical practice. Currently, extensive training is required for the reliable interpretation of confocal images. In addition, several reports indicate that small tumor foci are not consistently identified [7]. Therefore, the questions of the sensitivity and specificity, provided by confocal imaging should also be addressed. Highly specific markers, suitable for the *in vivo* use, could solve this problem. To the best of our knowledge there are no 100%-specific nontoxic contrast agents for human cancers available so far. There exist several specific immunohistochemical stains for nonmelanoma skin cancers that are used in histopathology [11,12]. However, all these stains are toxic and cannot be applied in humans *in vivo*.

In this contribution we investigated the feasibility of using dye-enhanced multimodal, reflectance, fluorescence, and fluorescence polarization confocal microscopy for the reliable detection of nonmelanoma skin cancers, that is, basal cell carcinoma (BCC) and squamous cell carcinoma (SCC). We used conventional histological stains, that is, methylene blue (MB) and toluidine blue (TB) that are nontoxic at low concentrations for tissue staining. These chromophores are not 100% cancer specific. However, they were reported to be preferentially retained in cancerous tissue [13,14]. TB and MB have been used in clinical practice for staining various carcinomas *in vivo* [15–19]. Our recent studies have shown that the staining pattern provided by these dyes in thick fresh skin excisions is remarkably similar to that of conventional hematoxylin and eosin (H&E) histopathology [6,20,21]. In this *in vitro*

Contract grant sponsor: ASLMS Ward Ford Memorial Grant.

*Correspondence to: Anna N. Yaroslavsky, PhD, MGH BAR 314B, 55 Fruit Street, Boston, MA 02114.

E-mail: yaroslav@helix.mgh.harvard.edu

Accepted 19 September 2007

Published online in Wiley InterScience

(www.interscience.wiley.com).

DOI 10.1002/lsm.20578

pilot trial we imaged fresh thick human nonmelanoma skin cancer specimens stained in TB or MB using multimodal confocal microscopy. Multi-spectral reflectance, fluorescence emission, and fluorescence polarization images were acquired and compared to H&E histopathology processed from the same tissue block with the goal of establishing the feasibility of using dye-enhanced multimodal confocal microscopy for diagnosing nonmelanoma skin cancers.

MATERIALS AND METHODS

Contrast Agents

Commercially available fluorescent dyes, that is, MB (MB 1% injection, USP, American Regent Laboratories, Inc., Shirley, NY) and TB (TB 1% AQ, LC26165-1, Fischer Scientific Company, Pittsburgh, PA) were used for staining. Both fluorophores belong to the family of phenothiazinium dyes. Absorption and fluorescence spectra of TB and MB are presented in Figure 1A and B, respectively. These dyes are conventional histological stains that are not toxic at low concentrations. TB is often considered the preferred histological stain for BCC [22,23].

Sample Preparation and Handling

Fresh tumor material was received from Mohs micrographic surgeries performed at the Dermatologic Surgery Unit of Massachusetts General Hospital. The experiments were performed according to a protocol approved by the Institutional Review Board of Massachusetts General Hospital. We used fresh skin excisions that were obtained within 40 minutes after Mohs micrographic surgeries. The tissue was briefly stained [up to 2 minutes] with 0.05 or 0.2 mg/ml DPBS solution of TB or MB, respectively. To remove dye excess the specimens were briefly rinsed [up to 5 minutes] in isotonic Dulbecco's phosphate-buffered solution (DPBS, pH 7.4). After staining, the tissue was imaged.

Confocal Microscopy and Image Processing

The schematic of the confocal microscope that was used for the experiments is presented in Figure 2. The microscope employs linearly polarized collimated light that is emitted by a He-Ne laser (633 nm) or diode lasers (656 nm and 830 nm). The excitation beam is directed onto the nonpolarizing beam splitter that provides 70% transmission and 30% reflection of the incident light in the wavelength range between 600 nm and 1,000 nm. The dichroic mirror is used to transmit the elastically scattered light and reflect the fluorescence emission coming from the sample. A narrow band pass filter (maximal transmission at 700 nm, full width at half maximum of 20 nm) is used in the fluorescence detection channel to further reject excitation light. The two orthogonal fluorescence polarization states are registered sequentially using a rotating linearly polarizing filter, a pinhole, and a photomultiplier tube. Thirty percent of the confocal reflectance signal from the sample is deflected by the 70/30 beam splitter, focused onto a pinhole, and registered by another photomultiplier tube. The system provides an axial resolution of 5–6 μm and a lateral resolution better than 1.2 μm in the range from 600 nm to 1,000 nm.

Reflectance, fluorescence, and fluorescence polarization of TB and MB were excited using 633 nm and 656 nm laser light, respectively. Reflectance images at 830 nm were acquired from all the specimens as a reference.

The confocal system may exhibit different efficiencies for the detection of different polarization states of the light. To enable accurate detection of the two orthogonally polarized components of fluorescence emission unbiased by the detection system, it was calibrated in a standard manner as described elsewhere [25]. The calibration factor, G, was found to be equal to 0.94.

Fluorescence polarization images of the tissues were calculated using the formula:

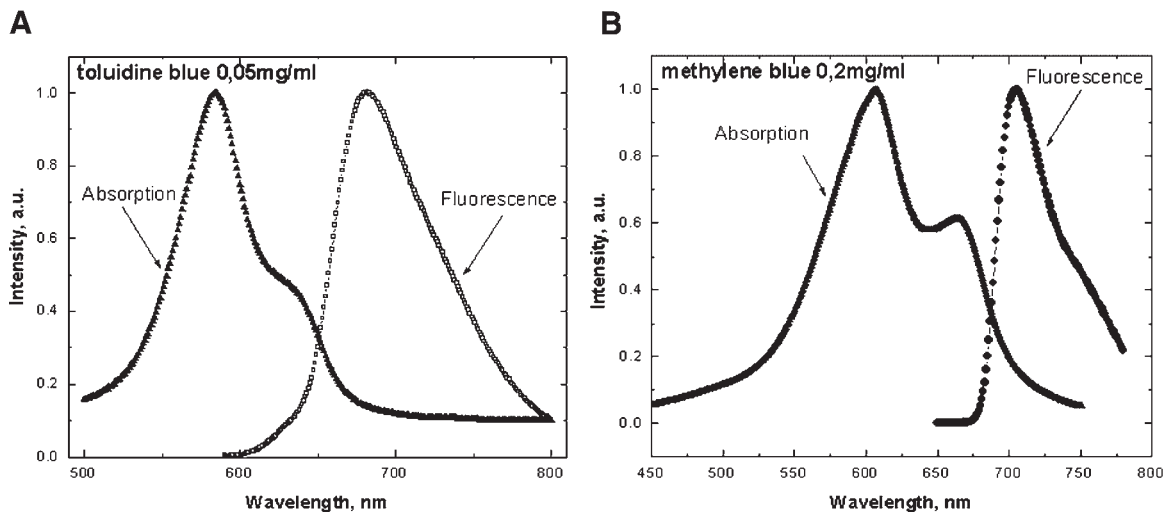


Fig. 1. Absorption and fluorescence of the aqueous solutions of (A) TB and (B) MB. TB was excited at 633 nm and MB was excited at 656 nm. Fluorescence and fluorescence polarization signals were registered between 690 and 710 nm.

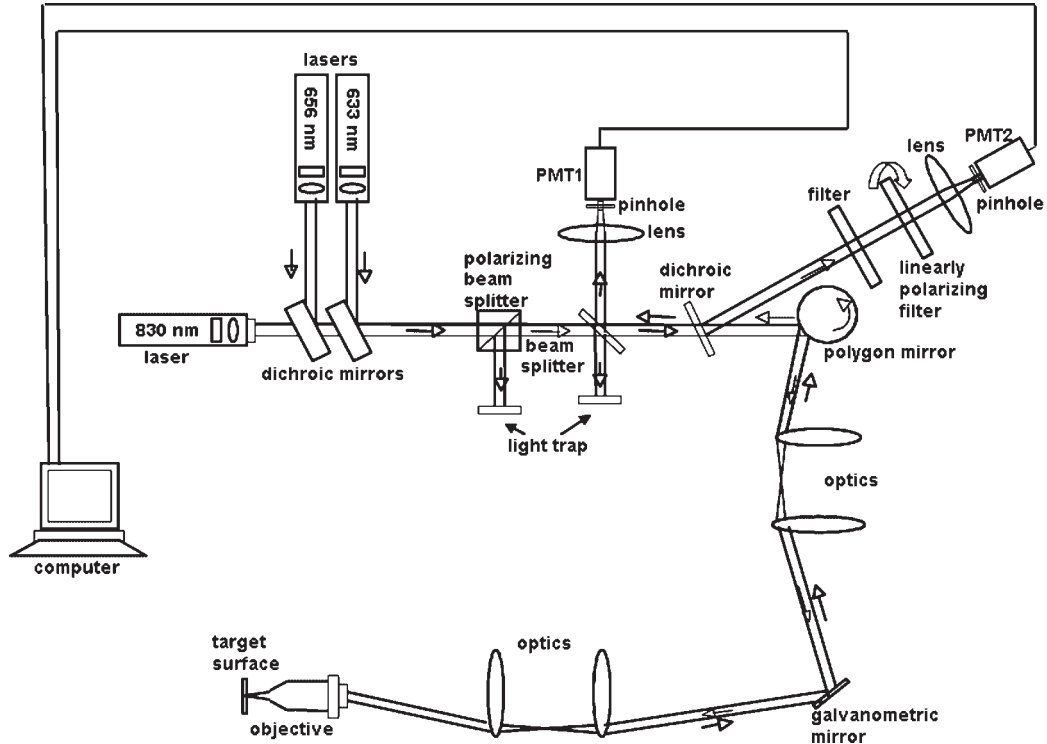


Fig. 2. Schematic of the confocal microscope.

$$F = 100 \times \frac{(F_{co} - G \times F_{cross})}{(F_{co} + G \times F_{cross})}$$

where F is a fluorescence polarization image, G is the calibration factor, F_{co} and F_{cross} are co- and cross-polarized fluorescence emission images, respectively.

Histopathology

Horizontal sections were prepared from the same tissue that was imaged in the following way. Tissue was frozen in an optimal cutting temperature compound and processed in the standard horizontal sectioning technique of Mohs [23,24]. Five micron-thick sections were transferred to glass slides and stained with hematoxylin and eosin. These frozen H&E sections were then compared to the confocal images obtained from approximately the same depth of the excision.

RESULTS AND DISCUSSION

In total, we have imaged 37 samples including 17 samples with nodular and micro-nodular BCC, 10 samples with infiltrative BCC, and 10 samples with invasive SCC. The resulting reflectance, fluorescence, and fluorescence polarization images were compared to the *en face* frozen H&E histopathological sections, processed from the same piece of tissue that was previously imaged. In all the cases the confocal images correlated well with the corresponding histopathology. Example images of nodular, infiltrative, and SCCs are presented in Figures 3–10.

In Figure 3 we compare the fluorescence (Fig. 3A) and reflectance (Fig. 3B–C,) confocal mosaics of a large (11 mm × 6.3 mm), thick (4 mm), fresh nodular BCC sample to the frozen H&E section (Fig. 3D) processed from the same tissue block. Figure 4 features the magnified images of tumor nodules. The sample was stained in 0.2 mg/ml aqueous solution of MB. It is worth noting that the ideal correlation of a confocal image and histology cannot be achieved because the image and the histological section cannot be acquired exactly from the same plane. Nonetheless, reflectance and fluorescence confocal mosaics, registered from the thick piece of cancerous skin, and an image of 5 μm thick histopathological section demonstrate similar features. In the images, “t” refers to cancer nodules, “e”—epidermis, “h”—to hair follicle, “l”—to fat tissue (lipids), “s”—to fibrous septa, “g”—to sebaceous gland, “i”—to inflammatory infiltrate, and *—to surgical suture.

The nodular (solid) type of BCC accounts for approximately 70% of all BCC cancers. In the H&E histopathology, this type of tumor is characterized by round or oval tumor islands of cells with peripheral palisading and unorganized central cells. The tumor cells usually have large, hyperchromatic, oval nuclei, and little cytoplasm. The cells are uniform, and mitosis, if present, is minimal. There is often an increased mucin content in the surrounding dermal stroma. Retraction spaces (cleft formation) can usually be observed between the islands and the stroma. Early nodular BCC lesions usually have some connection to the overlying epidermis.

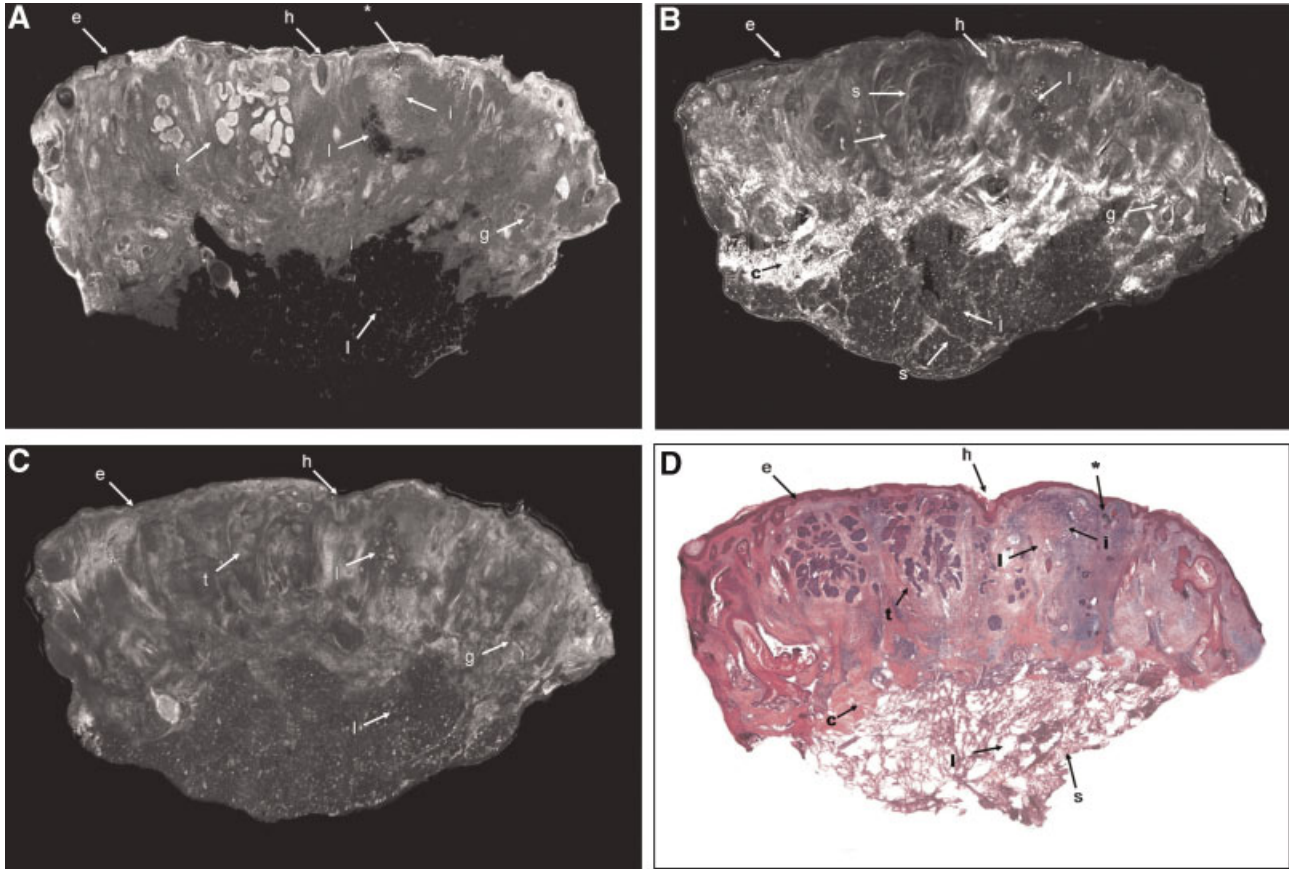


Fig. 3. Nodular BCC. Field of view 11.0 mm × 6.3 mm. (A) Fluorescence image. (B) Reflectance image at 656 nm. (C) Reflectance image at 830 nm. (D) H&E histopathology. In the images “e” refers to epidermis, “h”— to hair follicle, “l”— to fat tissue, “g” — to sebaceous gland, “i”—to inflammatory infiltrate, “s”— to septa, and “t”—to cancer nodules. “*” indicates surgical suture.

BCC tumor in the fluorescence image shown in Figure 3A can be distinguished from other structures by high fluorescence signal and its morphological appearance, similar to that of histopathology, presented in Figure 3D. Cancer is well demarcated from the benign epidermal and dermal structures. The stronger fluorescence of the peripheral cell layer as compared to the rest of the tumor, which can be clearly seen in the magnified fluorescence image of tumor nodules, as shown in Figure 4A, corresponds to the characteristic peripherally palisading cell pattern that is present in the histopathology examination (Fig. 4D).

High concentration of MB makes BCC nodules appear dark in the reflectance images acquired at 656 nm. High contrast of cancer islands helps in delineating it from other structures. Prominent trabeculae and septa separating BCC nests from each other, gives the tumor a unique three-dimensional (3D) appearance (see “s” in Fig. 3B). It allows for reliable discrimination of cancerous tissue. This 3D appearance cannot be observed in standard H&E histopathology. Thus, confocal imaging may improve current understanding of 3D structures of dermatopathological specimens and can also be used

for examination of 3D tumor invasion patterns. As a result, confocal microscopy may contribute to the differential diagnosis of malignant tumors. Images acquired at 656 nm correlate well with histopathology. However, in our opinion, the comparison of fluorescence images with H&E histopathology is more straightforward due to striking similarities in morphological appearance of the structures.

In confocal reflectance mosaics acquired at 830 nm nodular BCC appears lighter as compared to those acquired at 656 nm. This is to be expected, as MB does not absorb light at 830 nm. The tumor and other skin structures can be recognized at this imaging wavelength but are not demarcated well, as the overall contrast is lower in comparison with fluorescence (Figs. 3A, 4A) and 656 nm reflectance (Figs. 3B, 4B) images.

Example images of the infiltrative BCC specimen are shown in Figures 5 and 6. This is a large and thick specimen (18 mm × 8 mm × 5 mm). It was stained in 0.05 mg/ml aqueous solution of TB. Cancerous tissue is present in the central and right-hand side of the sample. In the images, “t” refers to infiltrative tumor strands, “e”—to epidermis, “h”—to hair follicle, “l”—to fat tissue (lipid), “m”—to

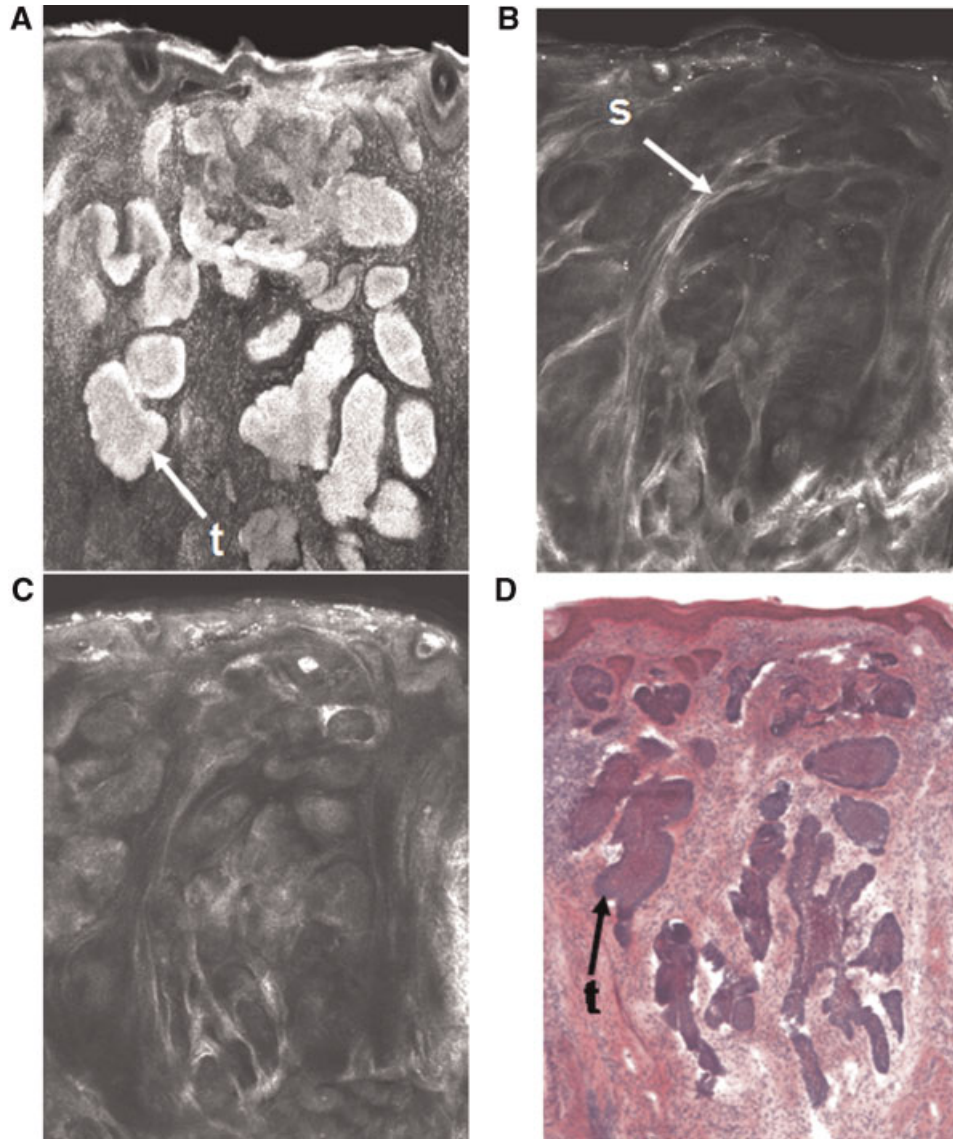


Fig. 4. Nodular BCC. Field of view 1.8 mm \times 2.2 mm. (A) Fluorescence image. (B) Reflectance image at 656 nm. (C) Reflectance image at 830 nm. (D) H&E histopathology. In the images “s” refers to septa and “t” — to cancer nodules.

arterial wall muscle, “g”—to sebaceous gland, and “f”—to fibrous stroma.

Infiltrative BCC is the most aggressive type of BCC with the highest potential for metastases. Upon H&E examination, infiltrative BCC is characterized by multiple small strands and nests that infiltrate the dermis and, in rare instances, the subcutaneous fat, and muscle. Those small 4–8 cell wide strands are composed of atypical basaloid cells arranged in an angulated spiky configuration. Peripheral palisading is rare and stromal retraction is minimal. The surrounding dermal stroma is fibrotic with minimal mucus and inflammatory infiltration. The tumor is poorly circumscribed. These features make histopathological diagnosis of infiltrative BCC somewhat challenging.

It has been reported in the literature [5,7] that detection of infiltrative BCC using acetic acid as a contrast agent and infrared reflectance confocal microscopy as an imaging technique is difficult. The problem arises because this type of BCC contains very thin strands of cancer cells imbedded within the dermis. Rinsing BCC tumors in acetic acid leads to enhanced scattering of cancerous cells [4]. At the same time, collagen exhibits intrinsically high scattering. Thus, reliable differentiation of infiltrative cancerous lesions, which reside in close proximity to collagen, is not feasible.

Example images presented in Figures 5 and 6 demonstrate that MB staining helps to solve the problem of detecting infiltrative BCCs. In the fluorescence images presented in Figures 5A and 6A, tumor strands of

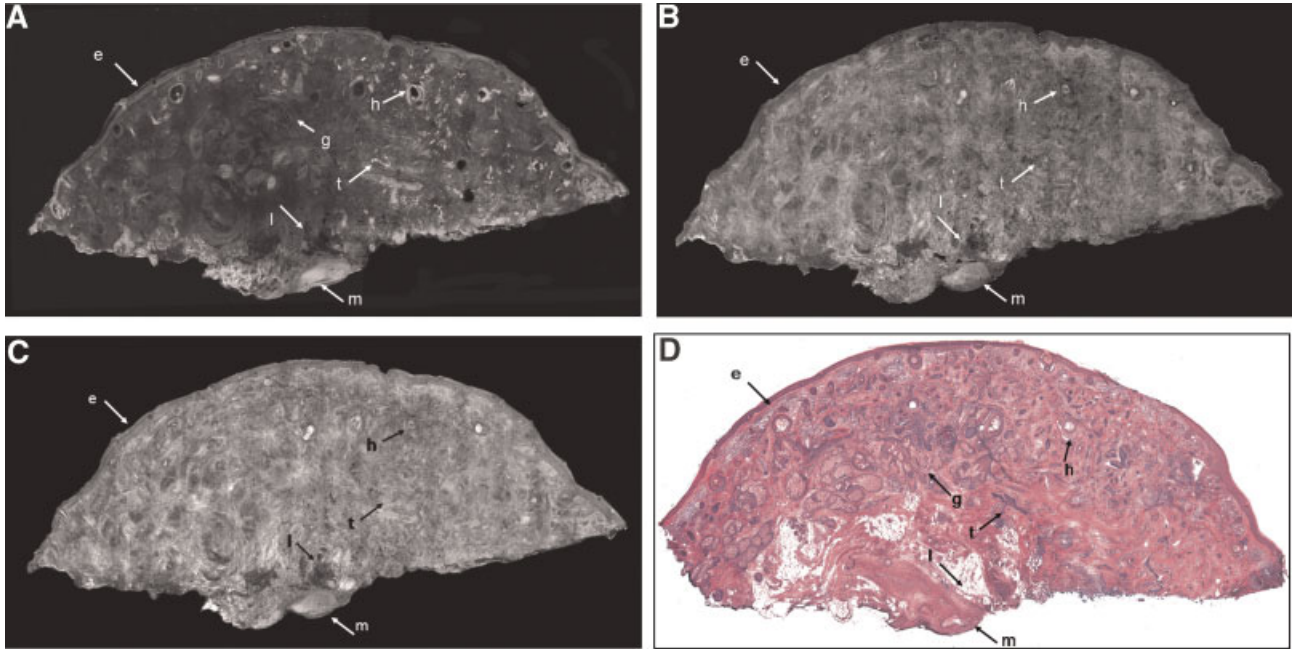


Fig. 5. Infiltrative BCC. Field of view 18.0 mm × 8.0 mm. (A) Fluorescence image. (B) Reflectance image at 633 nm. (C) Reflectance image at 830 nm. (D) H&E histopathology. In the images “e” refers to epidermis, “h” — to hair follicle, “l” — to fat tissue, “g” — to sebaceous gland, “m” — to the blood vessel muscle, and “t” — to infiltrating tumor strands.

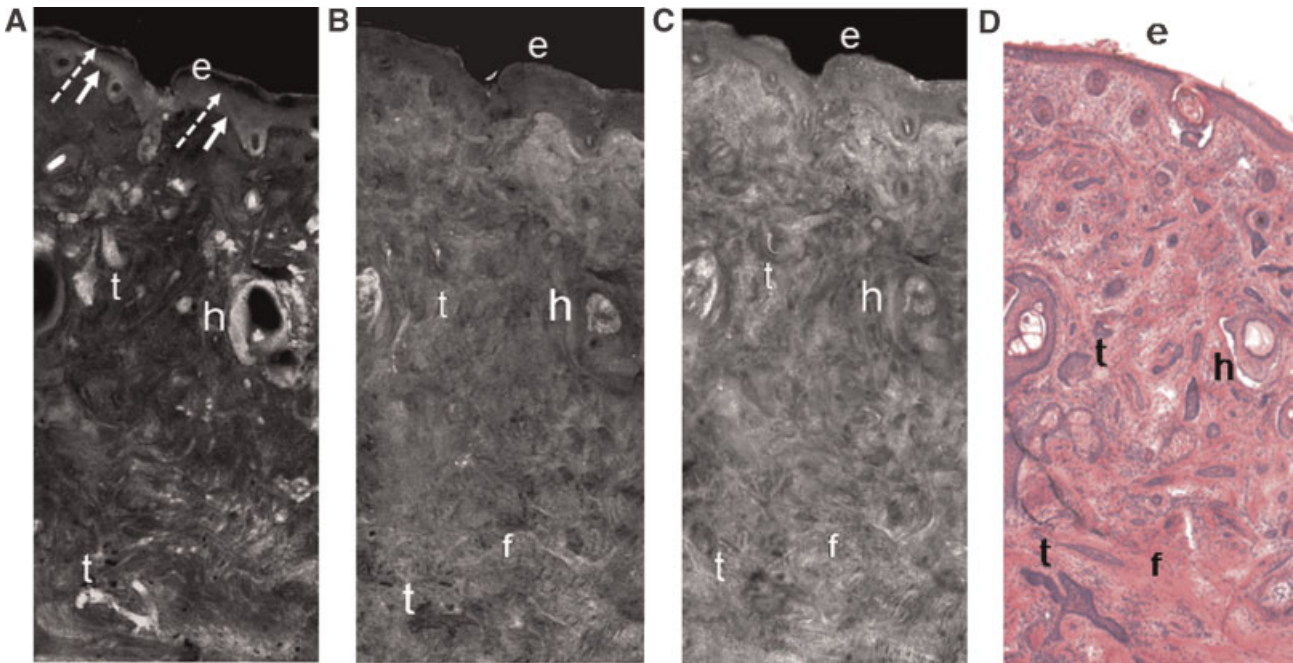


Fig. 6. Infiltrative BCC. Field of view 2.1 mm × 4.3 mm. (A) Fluorescence image. (B) Reflectance image at 633 nm. (C) Reflectance image at 830 nm. (D) H&E histopathology. In the images “e” refers to epidermis, “h” — to hair follicle, “f” — to fibrotic stromal response, and “t” — to infiltrating tumor strands. The dashed and solid arrows point towards the upper and the lower layers of epidermis, respectively.

morphea-form BCC are bright due to the high uptake of the MB. Surrounding collagen does not accumulate the dye and does not exhibit significant fluorescence in the wavelength range between 690 nm and 710 nm, as compared to MB. Infiltrative BCC is apparent in the image and can be distinguished from other structures by the infiltrative pattern within the dermis and surrounding the hair follicles. The characteristic small tumor strands and nests with their spiky configurations can be recognized by the high level of fluorescence in the magnified image of cancer affected part of the specimen presented in Figure 6A. They are marked in the image with “t”. Tumor appearance is similar to that in the histopathology examination shown in Figure 6D. The location and shape of the tumor nests in the fluorescence image correlate well with those in the histopathology. Thus, fluorescence confocal microscopy combined with MB staining is capable of detecting this complex sub-type of BCC.

In confocal reflectance mosaics excited at 633 nm and 830 nm, presented in Figure 5B and C, respectively, infiltrative BCC cannot be clearly delineated. However, the fibrotic stromal response can be recognized in the magnified images shown with “f” in Figure 6B and C.

In Figures 7 and 8, confocal images of the sample with invasive SCC are compared to H&E histopathology. This

comparatively large specimen (12 mm × 6.1 mm × 3 mm) was stained in a 0.2 mg/ml aqueous solution of MB. In the images, “t” refers to the islands of SCC, “e”—to epidermis, “h”—to hair follicle, and “g”—to sebaceous gland.

Invasive SCC is a malignancy of epidermal keratinocytes in which atypical keratinocytes extend from the epidermis into the dermis. They are arranged in elongated strands. Randomly oriented small nests of keratinocytes with varying shapes and sizes invade the dermis and form a reticular growth pattern (or an elongated stabbing pattern). Usually, there is a connection of the tumor to the epidermis.

In the fluorescence image presented in Figures 7A and 8A, invasive SCC is apparent and can be easily discriminated from other structures, as it exhibits high fluorescence. Dermal invasion and the stabbing growth pattern in the fluorescence images are manifested similarly to those in the H&E histopathology. There are some areas with epidermal continuity (shown with solid arrow in Fig. 8A) and irregular epidermal hyperplasia (shown with dashed arrow in Fig. 8A). The characteristic elongated strands and randomly oriented small cancer nests that invade the dermis and form a reticular growth pattern in H&E histopathology images (Figs. 7D, 8D) can also be found in the fluorescence images (Figs. 7A, 8A). The tumor in the confocal fluorescence image has well-defined margins.

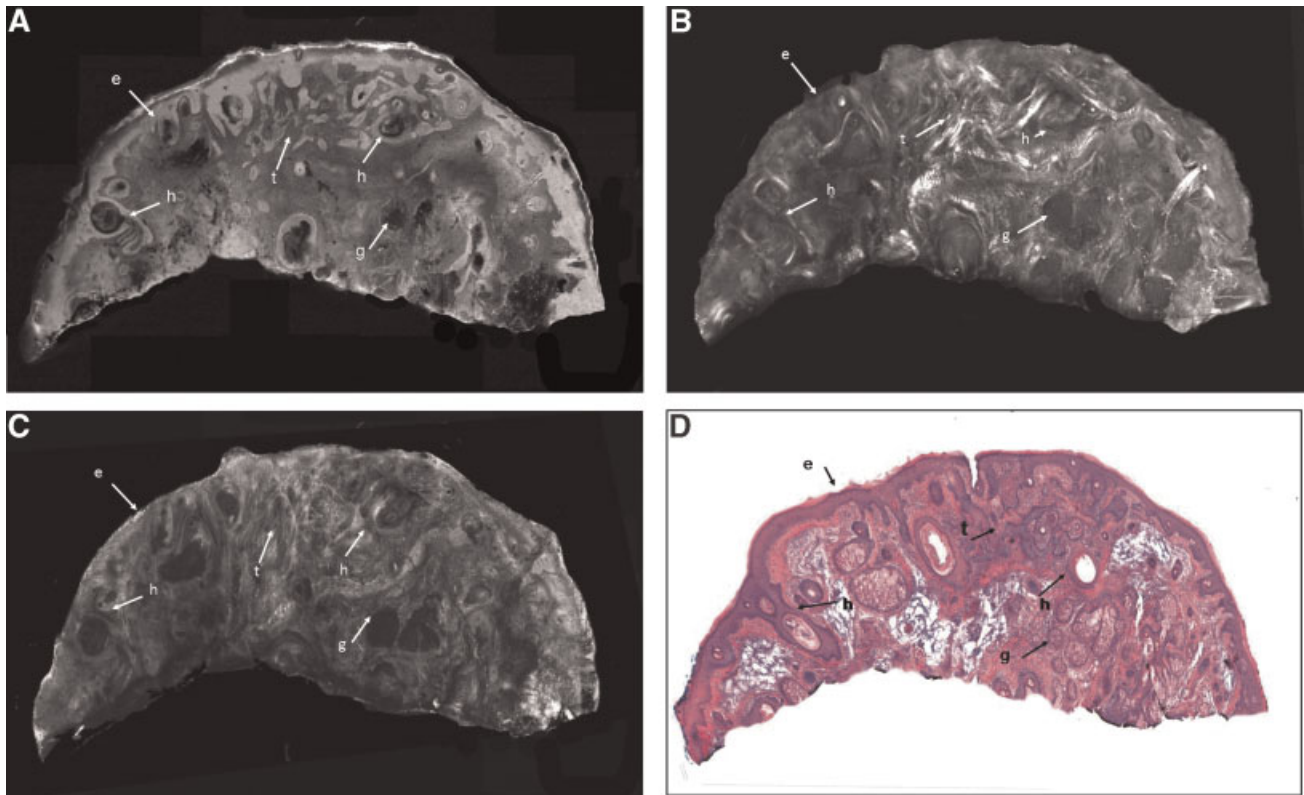


Fig. 7. Invasive SCC. Field of view 12.0 mm × 6.1 mm. (A) Fluorescence image. (B) Reflectance image at 656 nm. (C) Reflectance image at 830 nm. (D) H&E histopathology. In the images “e” refers to epidermis, “h”—to hair follicle, “g”—to sebaceous gland, and “t”—to tumor islands.

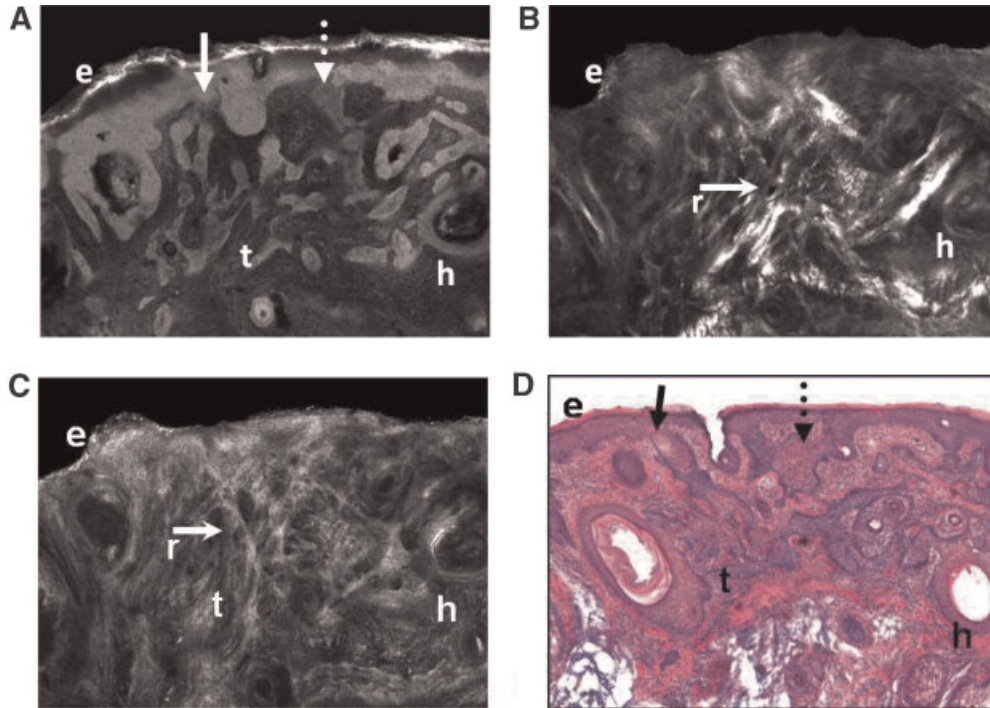


Fig. 8. Invasive SCC. Field of view $4.4 \text{ mm} \times 3.0 \text{ mm}$. (A) Fluorescence image. (B) Reflectance image at 656 nm. (C) Reflectance image at 830 nm. (D) H&E histopathology. In the images “e” refers to epidermis, “h” — to hair follicle, and “t” — to tumor islands, and “r” — to the reticular pattern. Solid arrow points towards the tumor areas of epidermal continuity and dashed arrow points toward the epidermal hyperplasia.

In the confocal reflectance mosaics acquired at 656 nm (see Figs. 7B, 8B) invasive SCC cannot be reliably differentiated from the other surrounding structures. Its stabbing pattern can be hardly appreciated because of the ill-defined tumor margins. Apparently, SCCs do not accumulate as much dye as BCCs, and consequently, are harder to delineate in the reflectance image, acquired within the absorption band of the dye.

In the confocal reflectance mosaic acquired at 830 nm, presented in Figures 7C and 8C, the stroma of invasive SCC appears as elongated bright islands that invade the dermis and form a reticular growth pattern (shown with “r” in Fig. 8C). The tumor exhibits continuity with the epidermis. The prominent elongated strands of this pattern, in Figure 8C, give it a unique three-dimensional (3D) appearance which cannot be seen in H&E histopathology. As in the case with nodular BCC, multimodal confocal imaging of SCC can be used for examination of 3D tumor invasion patterns and may contribute to the differential diagnosis of cancers.

Analysis of the benign structures present in the fluorescence images demonstrates that the lower layers, that is, stratum basale & stratum spinosum, of epidermis are brighter than the upper layer, stratum granulosum (see, e.g., Fig. 6A). In the images, the dashed and solid arrows point toward the upper and the lower layers of epidermis, respectively. In the fluorescence images (see, e.g., Figs. 6A,

7A) the hair follicles (indicated by “h”) and shafts appear similar to those in histopathology (see, e.g., Figs. 6D, 7D). Epidermal lining of the hair follicles can also be appreciated. These structures are less apparent in reflectance images. Similarly, in the fluorescence images in Figure 7A, the sebaceous glands (indicated by “g”) mimic the appearance of the same structure in histopathology, as shown in Figure 7D. The sebaceous glands in the reflectance images are dark and can be easily confused with the hair follicles (see, e.g., Fig. 7B,C). In contrast to the appearance of the hair follicles and sebaceous glands, collagen is bright in the reflectance image at 656 nm due to the high scattering of its fibers (see, e.g., Fig. 3B) and cannot be identified in fluorescence image (Fig. 3A). The subcutaneous fat tissue, indicated by “f”, appears as distinct groups of unique translucent black fat globules separated by prominent delicate fibrous septa, indicated by “s” (see Fig. 3B,C). Interestingly, in fluorescence images (Fig. 3A), in exact correlation with histopathology (Fig. 3D), we can see the trapped fat cells in the upper dermis, where the skin was biopsied for pathology confirmation prior to Mohs microsurgery. In fluorescence and histopathology images, presented in Figure 3A and D, respectively, in the upper dermis, where the biopsy was taken, we can recognize the surgical sutures surrounded by fibrous and scar tissue. In all confocal images the blood vessel muscle, indicated by “m” in Figure 5A–C, appears as a bright

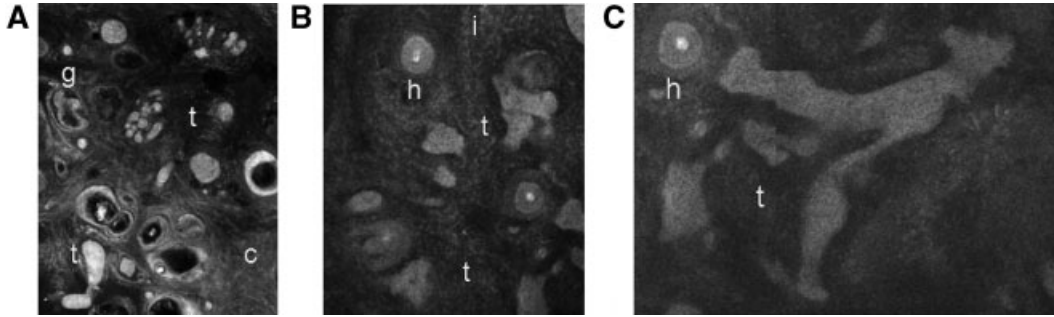


Fig. 9. Fluorescence emission images of (A) micro-nodular BCC, field of view $1.3 \text{ mm} \times 1.9 \text{ mm}$; (B) infiltrative BCC, field of view $1.3 \text{ mm} \times 1.9 \text{ mm}$, and (C) invasive SCC, field of view $1.7 \text{ mm} \times 1.4 \text{ mm}$. In the images “g” refers to sebaceous gland, “h” — to hair follicle, “c” — to collagen matrix, “i” — to inflammatory infiltrate, and “t” — to tumor islands.

longitudinal structure, deep in the dermis. Its shape and position correlates well with histopathology, as shown in Figure 5D. The inflammatory infiltration can be clearly detected in the fluorescence image in Figure 3A due to close correlation with histopathology presented in Figure 3D.

The results obtained using polarized light macro-imaging indicate that fluorescence polarization values registered from cancer are significantly higher than those obtained from normal skin structures [21]. However, in the macro-images observed higher values of fluorescence polarization from malignant tissue may be caused by the lower scattering coefficient of the latter. To investigate this phenomenon further, we have acquired confocal fluorescence polarization images and compared them with fluorescence emission images. Example images comparing fluorescence emission and fluorescence polarization for micro-nodular BCC, infiltrative BCC, and invasive SCC are presented in Figures 9A–C and 10A–C, respectively. All BCC specimens were stained in a 0.05 mg/ml aqueous solution of TB, whereas the SCC specimen was stained in a 0.2 mg/ml aqueous solution of MB. In the Figures 9 and 10, “t” refers to the tumor, “g”—to sebaceous gland, “h”—to hair follicle, “c”—to collagen matrix, and “i”—to inflammatory infiltrate. The Figure 9A–C demonstrate that several skin structures, such as the collagen matrix, hair follicles,

sebaceous glands, and inflammatory infiltrate, may appear similar to cancer in the fluorescence emission images. All these skin components and appendages uptake some dye and appear bright in fluorescence emission images. This ambiguity is resolved in the fluorescence polarization (FP) images. In the FP images shown in Figure 10A–C, malignant tissue is much brighter than other normal (sebaceous glands, hair follicles, and collagen) and pathological (inflammatory infiltrate) structures. The quantitative analysis of the images shown in Figure 10 confirms that the average values of fluorescence polarization in cancer equals to 0.27 ± 0.01 and is higher, as compared to collagen ($F = 0.18 \pm 0.01$), sebaceous glands ($F = 0.13 \pm 0.04$), inflammatory infiltrate ($F = 0.11 \pm 0.04$), and hair follicles ($F = 0.21 \pm 0.02$). Therefore, fluorescence polarization imaging of the tissues involved with cancer may provide the means for the reliable discrimination of malignancies.

CONCLUSIONS

To summarize, the data presented above strongly support the feasibility of using multimodal confocal microscopy in combination with the selected contrast agents, that is, MB and TB, for detecting nonmelanoma skin cancers and for guiding tumor excision surgery. The developed

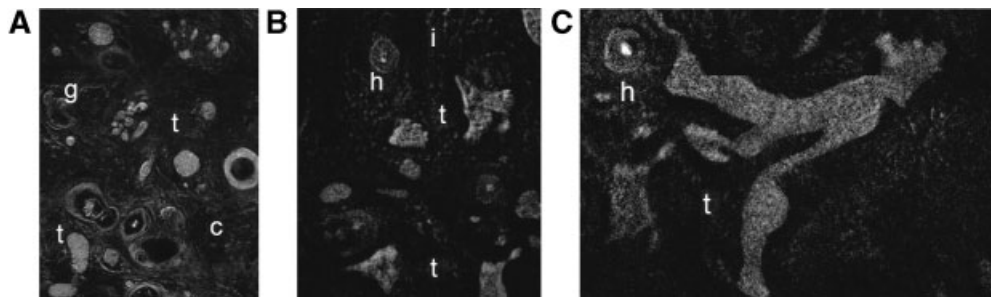


Fig. 10. Fluorescence polarization images of (A) micro-nodular BCC, field of view $1.3 \text{ mm} \times 1.9 \text{ mm}$; (B) infiltrative BCC, field of view $1.3 \text{ mm} \times 1.9 \text{ mm}$; and (C) invasive SCC, field of view $1.7 \text{ mm} \times 1.4 \text{ mm}$. In the images “g” refers to sebaceous gland, “h” — to hair follicle, “c” — to collagen matrix, “i” — to inflammatory infiltrate, and “t” — to tumor islands.

technique is capable of acquiring high quality images of SCCs and BCCs, including morphea form BCC. The fluorescence confocal images demonstrate that cancerous structures, stained using MB or/and TB, exhibit staining patterns similar to those of frozen H&E and are easily recognizable. As can be seen from the images presented in Figures 3–9, the appearance of healthy skin structures, such as the epidermis, collagen, hair follicles, sebaceous glands, and eccrine glands, is also similar in the optical and histopathology images. The data presented above indicate that fluorescence emission images mimic the morphological appearance of cancerous and normal skin structures in frozen H&E histopathology, whereas multi-spectral reflectance images provide complimentary information on the dye distribution and spectral responses of imaged tissues. We have shown that fluorescence polarization imaging has the potential to increase the sensitivity and specificity of confocal microscopy to detect skin cancers, due to the higher fluorescence polarization signal registered from malignant tissue as compared to other normal and pathological structures (see Fig. 10). MB and TB are nontoxic at low concentrations and safe for *in vivo* use. These dyes may be either applied topically or injected subcutaneously into the suspicious lesion. Therefore, future technological and clinical developments of multi-modal confocal microscopy may enable inspection of suspicious skin areas for the presence of cancer without invasive biopsy, whereas rapid acquisition of confocal images during cancer surgery may enable optical guidance of cancer treatments *in vivo* and in real time.

ACKNOWLEDGMENTS

We thank Dr. Victor Neel for providing skin specimens; Drs. Thomas Flotte, Victor Neel, and Zeina Tannous for validating our interpretation of confocal images; and Dr. R. Rox Anderson for the overall support of this project. Funding, provided by the ASLMS Ward Ford Memorial Grant, is gratefully acknowledged.

REFERENCES

1. González S, Tannous Z. Real-time, *in vivo* confocal reflectance microscopy of basal cell carcinoma. *J Am Acad Dermatol* 2002;47(6):869–874.
2. Nori S, Rius-Diaz F, Cuevas J, Goldgeier M, Jaen P, Torres A, Gonzalez S. Sensitivity and specificity of reflectance-mode confocal microscopy for *in vivo* diagnosis of basal cell carcinoma: A multicenter study. *J Am Acad Dermatol* 2004; 51:923–930.
3. Marghoob AA, Charles C, Busam KJ, Rajadhyaksha M, Lee G, Clark-Loeser L, Halpern AC. *In vivo* confocal laser scanning microscopy of a series of congenital melanocytic nevi suggestive of having developed malignant melanoma. *Arch Dermatol* 2005;141:1401–1412.
4. Tannous Z, Torres A, González S. *In vivo* real-time confocal reflectance microscopy: A non-invasive guide for Mohs micrographic surgery facilitated by aluminum chloride, an excellent contrast enhancer. *Dermatol Surg* 2003;29(8):839–846.

5. Rajadhyaksha M, Menaker G, Dwyer PJ, Flotte TJ, González S. Confocal examination of nonmelanoma cancers in skin excisions to potentially guide Mohs micrographic surgery without frozen histopathology. *J Invest Dermatol* 2001;117: 1137–1143.
6. Yaroslavsky AN, Barbosa J, Neel V, DiMarzio C, Anderson RR. Combining multi-spectral polarized-light imaging and confocal microscopy for localization of nonmelanoma skin cancer. *J Biomed Opt* 2005;10(1):014011.
7. Chung VQ, Dwyer PJ, Nehal KS, Rajadhyaksha M, Menaker GM, Charles C, Jiang SB. Use of *ex vivo* confocal scanning laser microscopy during Mohs surgery for nonmelanoma skin cancers. *Dermatol Surg* 2004;30(12):1471–1478.
8. Veiro JA, Cummins PG. Imaging of skin epidermis from various origins using confocal laser scanning microscopy. *Dermatology* 1994;189:16–22.
9. Rajadhyaksha M, Grossman M, Esterowitz D, Webb RH, Anderson RR. *In vivo* confocal scanning laser microscopy of human skin: Melanin provides strong contrast. *J Invest Dermatol* 1995;104:946–952.
10. Selkin B, Rajadhyaksha M, Gonzalez S, Langley RG. *In vivo* confocal microscopy in dermatology. *Dermatol Clin* 2001; 19369–19377.
11. Barnhill RL, Crowson AN, editors. *Textbook of Dermatopathology*. New York, NY: McGraw-Hill Companies, Inc; 2004. 575–633.
12. Elder DE, Elenitsas R, Johnson BL Jr, Murphy GF, editors. *Lever’s Histopathology of the Skin*. Philadelphia, PA: Lippincott Williams and Wilkins, Inc; 2005. 805–866.
13. Oseroff AR, Ohuoha D, Ara G, McAuliffe D, Foley J, Cincotta L. Intramitochondrial dyes allow selective *in vitro* photolysis of carcinoma cells. *Proc Natl Acad Sci USA* 1986;83:9729–9733.
14. Fukui I, Yokokawa M, Mitani G, et al. *In vivo* staining test with methylene blue for bladder cancer. *J Urol* 1983;130:252.
15. Eisen GM, Montgomery EA, Azumi N, Hartmann D-P, Bhargava P, Lippman M, Benjamin SB. Qualitative mapping of Barrett’s metaplasia: A prerequisite for intervention trials. *Gastrointest Endosc* 1999;50:814–818.
16. Fedorak IJ, Ko TC, Gordon D, Flisak M, Prinz RA. Localization of islet cell tumors of pancreas: A review of current techniques. *Surgery* 1993;113:242–249.
17. Gill WB, Huffman JL, Lyon ES, Bagley DH, Schoenberg HW, Straus FH II. Selective surface staining of bladder tumors by intravesical methylene blue with enhanced endoscopic identification. *Cancer* 1984;53:2724–2727.
18. Kaisary AV. Assessment of radiotherapy in invasive bladder carcinoma using *in vivo* methylene blue staining technique. *Urology* 1986;28:100–102.
19. Niebel HH, Chomet B. *In vivo* staining test for delineation of oral intraepithelial neoplastic change: Preliminary report. *JADA* 1965;68:801–805.
20. Yaroslavsky AN, Neel V, Anderson RR. Demarcation of nonmelanoma skin cancer margins using multi-spectral polarized-light imaging. *J Invest Dermatol* 2003;121:259–266.
21. Yaroslavsky AN, Neel V, Anderson RR. Fluorescence polarization imaging for delineating nonmelanoma skin cancers. *Opt Lett* 2004;29:2010–2012.
22. Humphreys TR, Nemeth A, McCrevey S, Baer SC, Goldberg LH. A pilot study comparing toluidine blue and hematoxylin and eosin staining of basal cell and squamous cell carcinoma during Mohs surgery. *Dermatol Surg* 1996;22: 693–697.
23. Gross KG, Steinman HK, Rapini RP, editors. *Mohs Surgery: Fundamentals and Techniques*. St. Louis: Mosby, Inc; 1999.
24. Mohs FE. Chemosurgery—A microscopically controlled method of cancer excision. *Arch Surg* 1941;42:279–295.
25. Lakowic JR. *Principles of Fluorescence Spectroscopy*. New York: Kluwer Academic/Plenum Publishers; 1999. pp. 298–299.